DESY 97-135
July 1997

Measurement of the Proton Structure Function F_2 and $\sigma_{tot}^{\gamma^* p}$ at Low Q^2 and Very Low x at HERA

ZEUS Collaboration

Abstract

A small electromagnetic sampling calorimeter, installed in the ZEUS experiment in 1995, significantly enhanced the acceptance for very low x and low Q^2 inelastic neutral current scattering, $e^+p \to e^+X$, at HERA. A measurement of the proton structure function F_2 and the total virtual photon-proton ($\gamma^* p$) cross-section is presented for $0.11 \leq Q^2 \leq 0.65$ GeV^2 and $2 \times 10^{-6} \leq x \leq 6 \times 10^{-5}$, corresponding to a range in the $\gamma^* p$ c.m. energy of $100 \leq W \leq 230$ GeV. Comparisons with various models are also presented.

The ZEUS Collaboration

J. Breitweg, M. Derrick, D. Krakauer, S. Magill, D. Mikunas, B. Musgrave, J. Repond, R. Stanek, R.L. Talaga, R. Yoshida, H. Zhang
Argonne National Laboratory, Argonne, IL, USA [p]

M.C.K. Mattingly
Andrews University, Berrien Springs, MI, USA

F. Anselmo, P. Antonioli, G. Bari, M. Basile, L. Bellagamba, D. Boscherini, A. Bruni, G. Bruni, G. Cara Romeo, G. Castellini[1], L. Cifarelli[2], F. Cindolo, A. Contin, M. Corradi, S. De Pasquale, I. Gialas[3], P. Giusti, G. Iacobucci, G. Laurenti, G. Levi, A. Margotti, T. Massam, R. Nania, F. Palmonari, A. Pesci, A. Polini, F. Ricci, G. Sartorelli, Y. Zamora Garcia[4], A. Zichichi
University and INFN Bologna, Bologna, Italy [f]

C. Amelung, A. Bornheim, I. Brock, K. Coböken, J. Crittenden, R. Deffner, M. Eckert, M. Grothe, H. Hartmann, K. Heinloth, L. Heinz, E. Hilger, H.-P. Jakob, U.F. Katz, R. Kerger, E. Paul, M. Pfeiffer, Ch. Rembser[5], J. Stamm, R. Wedemeyer[6], H. Wieber
Physikalisches Institut der Universität Bonn, Bonn, Germany [c]

D.S. Bailey, S. Campbell-Robson, W.N. Cottingham, B. Foster, R. Hall-Wilton, M.E. Hayes, G.P. Heath, H.F. Heath, D. Piccioni, D.G. Roff, R.J. Tapper
H.H. Wills Physics Laboratory, University of Bristol, Bristol, U.K. [o]

M. Arneodo[7], R. Ayad, M. Capua, A. Garfagnini, L. Iannotti, M. Schioppa, G. Susinno
Calabria University, Physics Dept.and INFN, Cosenza, Italy [f]

J.Y. Kim, J.H. Lee, I.T. Lim, M.Y. Pac[8]
Chonnam National University, Kwangju, Korea [h]

A. Caldwell[9], N. Cartiglia, Z. Jing, W. Liu, B. Mellado, J.A. Parsons, S. Ritz[10], S. Sampson, F. Sciulli, P.B. Straub, Q. Zhu
Columbia University, Nevis Labs., Irvington on Hudson, N.Y., USA [q]

P. Borzemski, J. Chwastowski, A. Eskreys, Z. Jakubowski, M.B. Przybycień, M. Zachara, L. Zawiejski
Inst. of Nuclear Physics, Cracow, Poland [j]

L. Adamczyk[11], B. Bednarek, K. Jeleń, D. Kisielewska, T. Kowalski, M. Przybycień, E. Rulikowska-Zarębska, L. Suszycki, J. Zając
Faculty of Physics and Nuclear Techniques, Academy of Mining and Metallurgy, Cracow, Poland [j]

Z. Duliński, A. Kotański
Jagellonian Univ., Dept. of Physics, Cracow, Poland [k]

G. Abbiendi[12], L.A.T. Bauerdick, U. Behrens, H. Beier, J.K. Bienlein, G. Cases[13], O. Deppe, K. Desler, G. Drews, U. Fricke, D.J. Gilkinson, C. Glasman, P. Göttlicher, J. Große-Knetter, T. Haas, W. Hain, D. Hasell, K.F. Johnson[14], M. Kasemann, W. Koch, U. Kötz, H. Kowalski, J. Labs, L. Lindemann, B. Löhr, M. Löwe[15], O. Mańczak, J. Milewski, T. Monteiro[16], J.S.T. Ng[17], D. Notz, K. Ohrenberg[18], I.H. Park[19], A. Pellegrino, F. Pelucchi, K. Piotrzkowski, M. Roco[20], M. Rohde, J. Roldán, J.J. Ryan, A.A. Savin, U. Schneekloth, F. Selonke, B. Surrow, E. Tassi, T. Voß[21], D. Westphal, G. Wolf, U. Wollmer[22], C. Youngman, A.F. Żarnecki, W. Zeuner
Deutsches Elektronen-Synchrotron DESY, Hamburg, Germany

B.D. Burow, H.J. Grabosch, A. Meyer, S. Schlenstedt
DESY-IfH Zeuthen, Zeuthen, Germany

G. Barbagli, E. Gallo, P. Pelfer
University and INFN, Florence, Italy [f]

G. Maccarrone, L. Votano
INFN, Laboratori Nazionali di Frascati, Frascati, Italy [f]

A. Bamberger, S. Eisenhardt, P. Markun, T. Trefzger[23], S. Wölfle
Fakultät für Physik der Universität Freiburg i.Br., Freiburg i.Br., Germany [c]

J.T. Bromley, N.H. Brook, P.J. Bussey, A.T. Doyle, D.H. Saxon, L.E. Sinclair, E. Strickland, M.L. Utley[24], R. Waugh, A.S. Wilson
Dept. of Physics and Astronomy, University of Glasgow, Glasgow, U.K. [o]

I. Bohnet, N. Gendner, U. Holm, A. Meyer-Larsen, H. Salehi, K. Wick
Hamburg University, I. Institute of Exp. Physics, Hamburg, Germany [c]

L.K. Gladilin[25], D. Horstmann, D. Kçira, R. Klanner, E. Lohrmann, G. Poelz, W. Schott[26], F. Zetsche
Hamburg University, II. Institute of Exp. Physics, Hamburg, Germany [c]

T.C. Bacon, I. Butterworth, J.E. Cole, V.L. Harris, G. Howell, B.H.Y. Hung, L. Lamberti[27], K.R. Long, D.B. Miller, N. Pavel, A. Prinias[28], J.K. Sedgbeer, D. Sideris, A.F. Whitfield[29]
Imperial College London, High Energy Nuclear Physics Group, London, U.K. [o]

U. Mallik, S.M. Wang, J.T. Wu
University of Iowa, Physics and Astronomy Dept., Iowa City, USA [p]

P. Cloth, D. Filges
Forschungszentrum Jülich, Institut für Kernphysik, Jülich, Germany

J.I. Fleck[5], T. Ishii, M. Kuze, M. Nakao, K. Tokushuku, S. Yamada, Y. Yamazaki[30]
Institute of Particle and Nuclear Studies, KEK, Tsukuba, Japan [g]

S.H. An, S.B. Lee, S.W. Nam[31], H.S. Park, S.K. Park
Korea University, Seoul, Korea [h]

F. Barreiro, J.P. Fernández, G. García, R. Graciani, J.M. Hernández, L. Hervás[5], L. Labarga, M. Martínez, J. del Peso, J. Puga, J. Terrón, J.F. de Trocóniz
Univer. Autónoma Madrid, Depto de Física Teórica, Madrid, Spain [n]

F. Corriveau, D.S. Hanna, J. Hartmann, L.W. Hung, J.N. Lim, W.N. Murray, A. Ochs, M. Riveline, D.G. Stairs, M. St-Laurent, R. Ullmann
McGill University, Dept. of Physics, Montréal, Québec, Canada [a], [b]

T. Tsurugai
Meiji Gakuin University, Faculty of General Education, Yokohama, Japan

V. Bashkirov, B.A. Dolgoshein, A. Stifutkin
Moscow Engineering Physics Institute, Moscow, Russia [l]

G.L. Bashindzhagyan, P.F. Ermolov, Yu.A. Golubkov, L.A. Khein, N.A. Korotkova, I.A. Korzhavina, V.A. Kuzmin, O.Yu. Lukina, A.S. Proskuryakov, L.M. Shcheglova[32], A.N. Solomin[32], S.A. Zotkin
Moscow State University, Institute of Nuclear Physics, Moscow, Russia [m]

C. Bokel, M. Botje, N. Brümmer, F. Chlebana[20], J. Engelen, P. Kooijman, A. van Sighem, H. Tiecke, N. Tuning, W. Verkerke, J. Vossebeld, M. Vreeswijk[5], L. Wiggers, E. de Wolf
NIKHEF and University of Amsterdam, Amsterdam, Netherlands [i]

D. Acosta, B. Bylsma, L.S. Durkin, J. Gilmore, C.M. Ginsburg, C.L. Kim, T.Y. Ling, P. Nylander, T.A. Romanowski[33]
Ohio State University, Physics Department, Columbus, Ohio, USA [p]

H.E. Blaikley, R.J. Cashmore, A.M. Cooper-Sarkar, R.C.E. Devenish, J.K. Edmonds, N. Harnew,
M. Lancaster[34], J.D. McFall, C. Nath, V.A. Noyes[28], A. Quadt, O. Ruske, J.R. Tickner, H. Uijterwaal,
R. Walczak, D.S. Waters
Department of Physics, University of Oxford, Oxford, U.K. [o]

A. Bertolin, R. Brugnera, R. Carlin, F. Dal Corso, U. Dosselli, S. Limentani, M. Morandin, M. Posocco, L. Stanco, R. Stroili, C. Voci
Dipartimento di Fisica dell' Università and INFN, Padova, Italy [f]

J. Bulmahn, R.G. Feild[35], B.Y. Oh, J.R. Okrasiński, J.J. Whitmore
Pennsylvania State University, Dept. of Physics, University Park, PA, USA [q]

Y. Iga
Polytechnic University, Sagamihara, Japan [g]

G. D'Agostini, G. Marini, A. Nigro, M. Raso
Dipartimento di Fisica, Univ. 'La Sapienza' and INFN, Rome, Italy [f]

J.C. Hart, N.A. McCubbin, T.P. Shah
Rutherford Appleton Laboratory, Chilton, Didcot, Oxon, U.K. [o]

D. Epperson, C. Heusch, J.T. Rahn, H.F.-W. Sadrozinski, A. Seiden, D.C. Williams
University of California, Santa Cruz, CA, USA [p]

O. Schwarzer, A.H. Walenta
Fachbereich Physik der Universität-Gesamthochschule Siegen, Germany [c]

H. Abramowicz, G. Briskin, S. Dagan[36], T. Doeker, S. Kananov, A. Levy[37]
Raymond and Beverly Sackler Faculty of Exact Sciences, School of Physics, Tel-Aviv University,
Tel-Aviv, Israel [e]

T. Abe, T. Fusayasu, M. Inuzuka, K. Nagano, I. Suzuki, K. Umemori, T. Yamashita
Department of Physics, University of Tokyo, Tokyo, Japan [g]

R. Hamatsu, T. Hirose, K. Homma, S. Kitamura[38], T. Matsushita, K. Yamauchi
Tokyo Metropolitan University, Dept. of Physics, Tokyo, Japan [g]

R. Cirio, M. Costa, M.I. Ferrero, S. Maselli, V. Monaco, C. Peroni, M.C. Petrucci, R. Sacchi, A. Solano, A. Staiano
Università di Torino, Dipartimento di Fisica Sperimentale and INFN, Torino, Italy [f]

M. Dardo
II Faculty of Sciences, Torino University and INFN - Alessandria, Italy [f]

D.C. Bailey, M. Brkic, C.-P. Fagerstroem, G.F. Hartner, K.K. Joo, G.M. Levman, J.F. Martin, R.S. Orr, S. Polenz, C.R. Sampson, D. Simmons, R.J. Teuscher[5]
University of Toronto, Dept. of Physics, Toronto, Ont., Canada [a]

J.M. Butterworth, C.D. Catterall, T.W. Jones, P.B. Kaziewicz, J.B. Lane, R.L. Saunders, J. Shulman, M.R. Sutton
University College London, Physics and Astronomy Dept., London, U.K. [o]

B. Lu, L.W. Mo
Virginia Polytechnic Inst. and State University, Physics Dept., Blacksburg, VA, USA [q]

J. Ciborowski, G. Grzelak[39], M. Kasprzak, K. Muchorowski[40], R.J. Nowak, J.M. Pawlak, R. Pawlak, T. Tymieniecka, A.K. Wróblewski, J.A. Zakrzewski
Warsaw University, Institute of Experimental Physics, Warsaw, Poland [j]

M. Adamus
Institute for Nuclear Studies, Warsaw, Poland [j]

C. Coldewey, Y. Eisenberg[36], D. Hochman, U. Karshon[36], D. Revel[36]
Weizmann Institute, Department of Particle Physics, Rehovot, Israel [d]

W.F. Badgett, D. Chapin, R. Cross, S. Dasu, C. Foudas, R.J. Loveless, S. Mattingly, D.D. Reeder, W.H. Smith, A. Vaiciulis, M. Wodarczyk
University of Wisconsin, Dept. of Physics, Madison, WI, USA [p]

S. Bhadra, W.R. Frisken, M. Khakzad, W.B. Schmidke
York University, Dept. of Physics, North York, Ont., Canada [a]

[1] also at IROE Florence, Italy
[2] now at Univ. of Salerno and INFN Napoli, Italy
[3] now at Univ. of Crete, Greece
[4] supported by Worldlab, Lausanne, Switzerland
[5] now at CERN
[6] retired
[7] also at University of Torino and Alexander von Humboldt Fellow at University of Hamburg
[8] now at Dongshin University, Naju, Korea
[9] also at DESY
[10] Alfred P. Sloan Foundation Fellow
[11] supported by the Polish State Committee for Scientific Research, grant No. 2P03B14912
[12] supported by an EC fellowship number ERBFMBICT 950172
[13] now at SAP A.G., Walldorf
[14] visitor from Florida State University
[15] now at ALCATEL Mobile Communication GmbH, Stuttgart
[16] supported by European Community Program PRAXIS XXI
[17] now at DESY-Group FDET
[18] now at DESY Computer Center
[19] visitor from Kyungpook National University, Taegu, Korea, partially supported by DESY
[20] now at Fermi National Accelerator Laboratory (FNAL), Batavia, IL, USA
[21] now at NORCOM Infosystems, Hamburg
[22] now at Oxford University, supported by DAAD fellowship HSP II-AUFE III
[23] now at ATLAS Collaboration, Univ. of Munich
[24] now at Clinical Operational Research Unit, University College, London
[25] on leave from MSU, supported by the GIF, contract I-0444-176.07/95
[26] now a self-employed consultant
[27] supported by an EC fellowship
[28] PPARC Post-doctoral Fellow
[29] now at Conduit Communications Ltd., London, U.K.
[30] supported by JSPS Postdoctoral Fellowships for Research Abroad
[31] now at Wayne State University, Detroit
[32] partially supported by the Foundation for German-Russian Collaboration DFG-RFBR (grant nos 436
RUS 113/248/3 and 436 RUS 113/248/2)
[33] now at Department of Energy, Washington
[34] now at Lawrence Berkeley Laboratory, Berkeley, CA, USA
[35] now at Yale University, New Haven, CT
[36] supported by a MINERVA Fellowship
[37] partially supported by DESY
[38] present address: Tokyo Metropolitan College of Allied Medical Sciences, Tokyo 116, Japan
[39] supported by the Polish State Committee for Scientific Research, grant No. 2P03B09308
[40] supported by the Polish State Committee for Scientific Research, grant No. 2P03B09208

[a] supported by the Natural Sciences and Engineering Research Council of Canada (NSERC)
[b] supported by the FCAR of Québec, Canada
[c] supported by the German Federal Ministry for Education and Science, Research and Technology (BMBF), under contract numbers 057BN19P, 057FR19P, 057HH19P, 057HH29P, 057SI75I
[d] supported by the MINERVA Gesellschaft für Forschung GmbH, the German Israeli Foundation, and the U.S.-Israel Binational Science Foundation
[e] supported by the German Israeli Foundation, and by the Israel Science Foundation
[f] supported by the Italian National Institute for Nuclear Physics (INFN)
[g] supported by the Japanese Ministry of Education, Science and Culture (the Monbusho) and its grants for Scientific Research
[h] supported by the Korean Ministry of Education and Korea Science and Engineering Foundation
[i] supported by the Netherlands Foundation for Research on Matter (FOM)
[j] supported by the Polish State Committee for Scientific Research, grant No. 115/E-343/SPUB/P03/002/97, 2P03B10512, 2P03B10612, 2P03B14212, 2P03B10412
[k] supported by the Polish State Committee for Scientific Research (grant No. 2P03B08308) and Foundation for Polish-German Collaboration
[l] partially supported by the German Federal Ministry for Education and Science, Research and Technology (BMBF)
[m] supported by the Fund for Fundamental Research of Russian Ministry for Science and Education and by the German Federal Ministry for Education and Science, Research and Technology (BMBF)
[n] supported by the Spanish Ministry of Education and Science through funds provided by CICYT
[o] supported by the Particle Physics and Astronomy Research Council
[p] supported by the US Department of Energy
[q] supported by the US National Science Foundation

1 Introduction

An early discovery at HERA was the rapid rise of the proton structure function, $F_2(x, Q^2)$, as the Bjorken scaling variable, x, decreases at low x for photon virtualities $Q^2 > 10$ GeV^2 [1, 2]. The ZEUS [3] and H1 [4] Collaborations have extended the measurement of F_2 down to a Q^2 value of 1.5 GeV^2. One of the most interesting features of the recent data is the persistence to the lowest Q^2 of the rapid rise of F_2 with decreasing x. The predictions of Glück, Reya and Vogt (GRV) [5], which result from the dynamic generation of parton densities via next-to-leading order (NLO) perturbative QCD (pQCD) DGLAP[6] evolution of valence type distributions starting at a very low scale, $Q_0^2 = 0.34$ GeV^2, are in broad agreement with this observation. It is surprising that leading twist NLO pQCD can describe the data down to $Q^2 = 1.5$ GeV^2. Other global fit analyses based on NLO pQCD, such as those performed by MRS [7] and CTEQ [8], typically have much higher starting scales $Q_0^2 = 3 - 5$ GeV^2. It then becomes an interesting question to determine at which Q^2 the behaviour of F_2 becomes dominated by non-perturbative contributions.

F_2 is related to the total virtual photon-proton ($\gamma^* p$) cross-section by $\sigma_{tot}^{\gamma^* p} \approx (4\pi^2\alpha/Q^2)F_2$ for $x \ll 1$. At fixed Q^2, the rapid rise of F_2 with decreasing x is equivalent to a rapid rise of the total $\gamma^* p$ cross-section with c.m. energy, W ($W^2 \approx Q^2/x$ in this kinematic regime). At high W, $\sigma_{tot}^{\gamma^* p}$ can be described by a power law behaviour, $\sigma_{tot}^{\gamma^* p} \propto W^{2\lambda}$. For $Q^2 \geq 1.5$ GeV^2, the power λ is between 0.15 and 0.35 [3, 4]. In contrast, the total cross-section for real photon-proton scattering (photoproduction, with $Q^2 = 0$) shows only a modest rise with W, $\lambda = 0.08$ [9], consistent with the energy behaviour of the total $p\overline{p}$ cross-section. Regge theory has been used successfully by, *e.g.,* Donnachie and Landshoff (DL) [9] to describe the energy dependence of the total cross-section for hadron-hadron scattering and real photon-proton scattering, but their prediction [10] for virtual photon-proton scattering fails to describe the data for $Q^2 \geq 1.5$ GeV^2. Different groups (CKMT[11], BK[12], ABY[13], and ALLM[14]) have used a variety of approaches to connect the very low Q^2 behaviour with high Q^2 pQCD. CKMT extend the Regge prediction by including Q^2 dependent absorptive corrections that modify the effective pomeron intercept, resulting in a Q^2 dependent λ up to some Q_0^2 in the range 1 to 5 GeV^2; pQCD is then used to evolve from this Q_0^2 to higher Q^2. BK describe the Q^2 behaviour using a generalised vector dominance model (GVDM): the low Q^2 region is controlled by the contributions of the low mass vector mesons, and the higher mass contributions are adjusted to provide agreement with pQCD predictions using a standard set of structure function parametrisations at larger Q^2. ABY extend their high Q^2 QCD-inspired parametrisation into the low Q^2 regime, and modify the evolution of α_s so that it saturates at a finite value. ALLM introduce parametrisations that interpolate between the Regge and pQCD regimes. A review is given in reference [15].

To study the transition from the hadronic type behaviour at $Q^2 \approx 0$ to the deep inelastic scattering (DIS) regime ($Q^2 \gg 1$ GeV^2), the kinematic coverage of the ZEUS detector was substantially extended starting in 1995 with the installation of a new beampipe calorimeter (BPC)[1]. Here we report on the measurement of F_2 and $\sigma_{tot}^{\gamma^* p}$ for $0.11 \leq Q^2 \leq 0.65$ GeV^2 from e^+p scattering at $\sqrt{s} = 300$ GeV using the ZEUS detector with the new BPC. This analysis is based on 1.65 pb^{-1} of data taken during the 1995 HERA run. Recently the H1

[1]The new BPC replaced a previous calorimeter described in [16].

Collaboration has reported an F_2 measurement in four bins in the Q^2 range of 0.35 to 0.65 GeV^2 in a somewhat different W range [17]. For $Q^2 \geq 0.23$ GeV^2, the E665 Collaboration reported a measurement of the proton structure function at much higher x[18] than this analysis.

2 Kinematics

Inelastic positron-proton scattering,

$$e^+p \to e^+X \tag{1}$$

can be described in terms of two kinematic variables, x and Q^2, where x is the Bjorken scaling variable and Q^2 the negative of the square of the four-momentum transfer. In the absence of initial and final state radiation, $Q^2 = -q^2 = -(k-k')^2$ and $x = Q^2/(2P\cdot q)$, where k and P are the four-momenta of the incoming positron and proton respectively and k' is the four-momentum of the scattered positron. The fractional energy transfer to the proton in its rest frame, y, can be related to x and Q^2 by $y = Q^2/(sx)$, where s is the square of the e^+p c.m. energy which is given by $s \simeq 4E_eE_p$. Here, E_e (27.5 GeV) and E_p (820 GeV) are the positron and proton beam energies, respectively. The kinematic variables, y and Q^2, are related to the energy, E'_e, and angle with respect to the proton beam direction, θ_e, of the scattered positron. We also use $\vartheta = \pi - \theta_e$, the angle with respect to the positron beam direction. Scattering at low Q^2 results in positrons emerging at small ϑ,

$$y = 1 - \frac{E'_e}{2E_e}(1+\cos\vartheta) \approx 1 - \frac{E'_e}{E_e}, \quad Q^2 = 2E_eE'_e(1-\cos\vartheta) \approx E_eE'_e\vartheta^2. \tag{2}$$

3 Experimental setup and kinematic reconstruction

The ZEUS detector [19] is a general purpose magnetic detector at the HERA collider. To enhance the acceptance of the detector at small Q^2, two beam pipe calorimeter modules (BPC) [20] located on two sides of the beam pipe at 2937 mm from the interaction point in the rear (positron) direction[2] were installed, as shown in figure 1(a). The BPC covers positron scattering angles relative to the incident direction of 15 to 34 mrad. At these small angles, the maximum possible scattered positron energy is equal to the beam energy, 27.5 GeV. The beam pipe has two low-mass windows (0.016 radiation length (r.l.)) in front of the BPC to allow positrons to exit the beam pipe with minimal interference.

The BPC is an electromagnetic scintillator sampling calorimeter. The passive absorber layers consist of twenty-six 13.8 cm $\times$ 13 cm $\times$ 0.92 r.l. thick tungsten alloy plates; the active layers consist of 7.9 mm wide and 2.6 mm thick scintillator strips alternating each

[2]The ZEUS right-handed coordinate system is defined with the origin at the nominal interaction point by the Z axis pointing in the proton beam direction and the X axis horizontally pointing towards the center of HERA.

layer in the horizontal and vertical directions. The scintillator strips are read out from one end using wavelength shifters (WLS). Each WLS is coupled to a miniature photomultiplier tube (Hamamatsu R5600-03). The vertically oriented scintillator strips provide the X position measurement and the horizontally oriented strips the Y measurement. The readout electronics are similar to those used for the main ZEUS uranium scintillator calorimeter (CAL) [19]. The alignment is known to an accuracy of 0.5 mm from an optical geometrical survey. The distance between the two calorimeter modules on either side of the beam pipe is mechanically constrained to within 0.2 mm. Due to synchrotron radiation from the positron beam, the modules are placed asymmetrically around the beam. Only one of the two BPC modules is used for physics analysis due to the very small acceptance of the other module, which is used exclusively for alignment purposes. The typical geometrical acceptance is 10%.

3.1 Detector simulation and response

The BPC simulation is based on the GEANT [21] program, with an independent check performed using EGS4 [22]. The energy spectra for 1 to 6 GeV incident electrons in the simulation are in good agreement with test beam data taken at these energies, and are consistent with the design energy resolution of $17\%/\sqrt{E}$. The non-linearity is found to be less than 1% in the simulation for 2 to 6 GeV incident electrons, in agreement with test beam data.

The energy calibration was performed *in situ* using *kinematic peak* (KP) events[3] in two steps: a relative strip-to-strip calibration, followed by an overall energy scale calibration. Figure 1(b) shows the fractional deviation of the KP energy from the mean value as a function of the scattered positron X impact position at the BPC after the relative calibration. The energy scale is uniform to within 0.5% over the BPC fiducial region, which extends to 8 mm from the edge of the BPC. The overall energy scale was established by comparing the KP energy spectra of data and simulation, which included QED radiative corrections. A χ^2 was calculated between the two spectra, and the energy scale of the data adjusted to minimise it.

The absolute energy scale obtained with KP events was checked using elastic ρ^0 events, $e^+p \to e^+\rho^0 p$. The scattered positron energy and position were measured in the BPC, and the three-momenta of the two ρ^0 decay pions were measured using the ZEUS Central Tracking Detector (CTD)[24]. Using the four-momentum of the ρ^0, the scattered positron energy can be independently determined. Figure 1(c) shows the ratio of the measured positron energy to that determined from the CTD, for both simulation and data. Radiative corrections are responsible for the tail at low values and the fact that the distributions peak below unity. The agreement between the data and the simulation is very good. Consequently, it was concluded that the energy scale determined using the KP events was accurate to within 0.5%, and that the BPC resolution was well modeled in the simulation.

The BPC was located only 4.4 cm from the beam in the horizontal direction, and received

[3] A cut $y_{JB} < 0.04$ (see below) selects scattered positrons whose energy distribution sharply peaks within 2% of the beam energy, providing a good calibration source [23].

12 kGy of radiation during the 1995 HERA running period. The resulting damage caused a drop in the energy scale of up to 2.5% for the regions closest to the beam, determined using KP events. To correct for this, the data were separated into 4 time periods and the energy calibration performed separately for each period. The amount of radiation damage to the BPC was also determined using a movable cobalt source scan calibration system [25] and by measuring the response of a sample of scintillator strips after disassembling the calorimeter at the end of 1995 after data taking. The degradation of each individual scintillator strip was built into the EGS4 simulation, which showed that the non-linearity from 10 GeV to full scale due to radiation damage was less than 1%.

The BPC measured the arrival time of the positron with an accuracy determined to be 0.4 ns for positrons with an energy greater than 6 GeV.

3.2 Positron identification and position reconstruction

The scattered positron position in the BPC was determined using the logarithmic energy-weighted shower position [26] using scintillator strips containing more than 4% of the total shower energy. A RMS resolution of 1.3 mm with a maximum systematic shift of 0.5 mm was obtained for 5 GeV incident electrons in the beam test. This was well-reproduced in the simulation. The position resolution improves gradually with increasing positron energy. The resolution was determined from the simulation to be 0.6 mm at 27.5 GeV for positron impact positions within the fiducial region of the BPC.

As a cross-check of the absolute position, QED Compton events $e^+p \to e^+\gamma p$ were used. Since both the photon and the scattered positron are detected in the BPC modules, these events provide an over-constrained kinematic system. Using the accurately known distance between the two BPC modules and the QED Compton event kinematics, the position of each BPC module relative to the positron beam was determined. The agreement with the survey is better than 0.5 mm. The accuracy of the QED Compton method is dominated by the uncertainty of the calorimeter energy scale: 0.5%, corresponding to 0.5 mm.

Positron identification was performed using the transverse size of the shower. The second moments of the shower in the X and Y directions, σ_X and σ_Y, were calculated using the logarithmic energy weighted method mentioned above. The combination $\sqrt{(\sigma_X^2 + \sigma_Y^2)/2}$ was required to be less than 7.5 mm. This yielded a positron acceptance in excess of 95% at 7 GeV, rising to 98% above 12 GeV, while rejecting hadrons and positrons that have preshowered in the beam-pipe wall, which have a much wider transverse width. Using a sample of KP positrons, the transverse energy profile in the simulation was tuned to that of the data.

3.3 Vertex determination and luminosity measurement

The position of the e^+p interaction vertex is needed to determine the positron scattering angle. The Z position of the vertex was measured using the CTD on an event-by-event basis with a typical resolution of 4 mm. For events with no CTD vertex information

(about 8% of the total), the Z position of the vertex was set to the average position of the full data sample, <Z> = −3 cm. The longitudinal size of the luminous region was about 12 cm (r.m.s.). The mean values of the X and Y vertex positions, determined on a run-by-run basis, were used. The transverse sizes of the beam in X and Y were about 300 μm and 70 μm, respectively.

The luminosity was measured via the bremsstrahlung process $e^+p \rightarrow e^+\gamma p$, using a separate electromagnetic calorimeter detector system (LUMI) [27]. A lead-scintillator calorimeter positioned at Z = −107 m, accepting photons with scattering angles less than 0.5 mrad, was used for the luminosity measurement. The uncertainty of the luminosity measurement for the data sample used in this analysis is 1.5%. A second electromagnetic calorimeter, positioned at Z = −35 m, was used for tagging positrons in background studies.

3.4 Reconstruction of the kinematic variables

In this analysis, the kinematic variables y and Q^2 are reconstructed using the energy and angle of the scattered positron, determined using the BPC and the CTD vertex position with equation 2. Using this method of reconstruction ("electron method"), y and Q^2 can be determined reliably over the kinematic range $y > 0.1$ and $Q^2 > 0.1$ GeV^2. The y resolution is 0.02 to 0.04, and the Q^2 resolution is 6 to 8%.

As the ZEUS CAL is an almost hermetic detector, it can be used to measure the hadronic system, denoted by X in equation 1. The following quantities are reconstructed using the CAL,

$$\delta_{CAL} = \sum_i E_i(1 - \cos\theta_i), \quad y_{JB} = \frac{\delta_{CAL}}{2E_e}, \quad E_{tot} = \sum_i E_i, \tag{3}$$

where E_i is the energy measured in the i^{th} CAL cell and θ_i is the polar angle of the center of the i^{th} calorimeter cell with respect to the positive Z axis; the sum extends over all cells in the CAL. The quantity y_{JB} provides a measure of the kinematic variable y, and has superior resolution at very low y compared to that from the electron method. E_{tot} is the measured total energy of the hadronic system. These quantities were used in the trigger and event selection for rejecting background, reducing QED radiative corrections and controlling event migration at low y.

4 Trigger, data taking and event selection

ZEUS selects events online using a three-level trigger system [28]. Both the energy and timing information from the BPC were used for the First Level Trigger (FLT). An energy cut of 6 GeV was made and the timing was required to be consistent with an e^+p collision. Proton-gas events occurring upstream were also rejected by timing measurements made by scintillation counter arrays situated along the beamline at $Z = -730, -315$, and -150 cm,

respectively. For the Second Level Trigger, CAL timing information was used to reject non e^+p events. An approximate value of y_{JB}, determined from the CAL energies assuming an interaction vertex at Z = 0, was required to be greater than 0.02 and the total CAL energy was required to be greater than 3 GeV. No additional BPC cuts were imposed at the Third Level Trigger.

The FLT efficiency was studied using a sample of events triggered only by the CAL. All of the offline event selection cuts (see below) were applied to this sample. The trigger was found to be fully efficient for BPC energies greater than 7 GeV, as shown in figure 1(d).

The offline event selection cuts are as follows. The reconstructed positron is required to be within the BPC fiducial region, to have more than 7 GeV energy, and to pass the shower width cut described in section 3.2. The BPC time is required to be within 3 ns of the time for e^+p interactions. If the event vertex is well reconstructed with the CTD, the Z position of the vertex is required to be within the window -40 cm $< Z_{VTX} <$ 100 cm. The quantity $\delta = \delta_{CAL} + 2E'_e$, is required to lie in the range 35 to 60 GeV; δ equals twice the positron beam energy (55 GeV) for a completely contained event, but the distribution peaks at much lower values for photoproduction events where the scattered positron is lost in the rear direction. A cut y_{JB} >0.06 reduces migration of events from very low y, where the resolution of the electron method is poor. Finally, if timing information from the CAL is available, the time is required to be consistent with an e^+p collision. After cuts, 109105 events remain in the data sample.

5 Analysis

5.1 Physics simulation

A physics simulation is used to determine the radiative corrections and the acceptance of the detector. The starting point for the simulation of e^+p collisions in the y and Q^2 region of this measurement is the program DJANGO 6.22, which interfaces the programs HERACLES [29] 4.5.1, ARIADNE [30] 4.06 and LEPTO [31] 6.4.1. The HERACLES program calculates the structure functions F_2 and F_L from an input set of parton density functions. From these, it calculates the differential cross-section including initial and final state radiation, and the full one-loop virtual corrections. ARIADNE implements the colour dipole model for gluon radiation between the struck quark and the proton remnant. Finally, LEPTO handles the fragmentation using the program JETSET [32].

Several modifications were made to the program to generate events at low Q^2. (1) The Donnachie-Landshoff parameterisation [10] was used to calculate F_2 in the Q^2 range of this measurement.
(2) The longitudinal structure function F_L was set equal to zero at this stage. (3) Elastic vector meson (VM) ρ^0 events were generated. The VM events were re-weighted according to the cross-section and W dependence recently measured at ZEUS using the BPC. This contribution amounted to 6% of the events [33]. (4) Diffractive events were generated according to $d^2\sigma/dtdM_X^2 \sim e^{bt}/(M_X^2 + Q^2 - M_\rho^2)^{1.1}$ [34], where t is the square of the four-momentum transferred to the outgoing proton, M_X is the invariant mass of the

hadronic final state, and $b = 6$ GeV^{-2}. The fraction of diffractive events (around 25%) was determined from the data by counting the events with a characteristic rapidity gap; that is, a region of little or no hadronic activity between the forward edge of the CAL and the jet from the struck quark. The overall acceptance is weakly sensitive to changes in the relative contributions of the different event types (see section 5.5).

A generated event sample in the region $Q^2 > 0.05$ GeV^2 and $y > 0.03$ corresponding to more than twice the luminosity of the data was passed through the complete ZEUS simulation chain, which is based on the GEANT [21] program, and then processed using the same offline reconstruction software as for the data. The general characteristics of the data are well-described by the simulation, as shown in figure 2(a-c).

5.2 Binning of the data

The data are binned in the variables y and Q^2, which makes efficient use of the available phase space, as the lower electron energy cut corresponds to an upper y cut. The accessible kinematic region lies between y values of 0.08 and 0.74, and Q^2 values of 0.1 and 0.74 GeV^2. The sizes of the bins are chosen based on the experimental resolution of the kinematic variables and the number of events. At low y, the bin widths in y are chosen to be twice the y resolution; for y greater than 0.37, bins of approximately constant width are used. The lowest Q^2 bin has a width 2.5 times the Q^2 resolution; higher Q^2 bins have a constant width in $\log(Q^2)$ which results in approximately constant numbers of events in each Q^2 interval.

For positrons within the BPC fiducial region, the efficiency of the event selection cuts is close to 100% for $y < 0.5$, decreasing to about 70% at $y = 0.7$. The purity, defined as the fraction of events reconstructed in a bin that were generated in that bin, is typically 50%.

5.3 Background determination

The background from beam-gas interactions is determined using unpaired positron and proton bunches. The size of this background is 1%, and is subtracted statistically. The dominant source of background comes from photoproduction interactions where the scattered positron escapes through the rear beam pipe and a fake positron is reconstructed in the BPC. Typically such events have much lower δ values than signal events. Photoproduction background events were generated using the PYTHIA program [35] with the ALLM cross-section parameterisation [14]. This PYTHIA sample is used to perform a bin by bin subtraction of the photoproduction background. Figure 2(d) shows the δ spectra for data (solid circles), signal simulation (dashed line), photoproduction simulation (shaded region), and the sum of the signal and photoproduction simulations (solid line). The good agreement between this sum and the data suggests that the photoproduction background is well simulated, and gives a contamination of a few percent in most bins, rising up to 15% in the highest y bins.

As a cross-check, use was made of the very small angle LUMI positron detector to measure the photoproduction background directly. This detector accepts scattered positrons with

$Q^2 < 0.01$ GeV^2 and $0.2 < y < 0.6$ and may be used to tag events with a fake BPC positron signal that pass the event selection cuts. The measured background is shown as the triangular points in figure 2(d); the $y < 0.6$ cut limits the measurement to $\delta < 35$ GeV. Once again, the measured points are in good agreement with the simulated background.

The contamination from higher Q^2 DIS events is less that 0.1% based on searches in the CAL for additional positron candidates in both data and the simulation.

5.4 Determination of F_2 and $\sigma_{tot}^{\gamma^* p}$

The double-differential e^+p cross-section for inelastic scattering can be expressed in terms of the total cross-section for virtual transverse (T) and longitudinal (L) photons:

$$\frac{d^2\sigma(ep \to eX)}{dydQ^2} = \Gamma \left[\sigma_T(y,Q^2) + \epsilon\sigma_L(y,Q^2)\right](1+\delta_r(y,Q^2)) \qquad (4)$$

where the flux $\Gamma \approx \alpha(1+(1-y)^2)/(2\pi Q^2 y)$, the fractional flux of longitudinally polarised virtual photons $\epsilon \approx 2(1-y)/(1+(1-y)^2)$, and δ_r is the radiative correction factor. These cross-sections can be related to the proton structure functions F_2 and F_L by $F_2 = (Q^2+4m_p^2x^2)(\sigma_T+\sigma_L)/(4\pi^2\alpha(1-x))$, $F_L = (Q^2+4m_p^2x^2)\sigma_L/(4\pi^2\alpha(1-x))$ and the total virtual photon-proton cross section by $\sigma_{tot}^{\gamma^* p} \equiv \sigma_T + \sigma_L$. In the Q^2 range of this analysis, the contribution from Z^0 exchange is negligible. The radiative correction to the Born cross-section, δ_r, is a function of y and Q^2, but to a good approximation is independent of F_2.

An iterative procedure is adopted to extract the sum $\sigma_T + \epsilon\sigma_L$. Monte Carlo events are generated as described in section 5.1 to determine the acceptance and efficiency of the cuts in each bin. The first $\sigma_T + \epsilon\sigma_L$ values are then fit with a simple functional form, inspired by the ALLM parameterisation [14]. The result of the fit is used to reweight the input distributions in the simulation event by event to re-evaluate the acceptance and efficiency. New values of $\sigma_T + \epsilon\sigma_L$ in each bin are calculated and the procedure repeated until the change between subsequent iterations is less than 0.5% in all bins; three iterations are required. The relative fractions of diffractive and VM events are kept fixed in this procedure.

Once the $\sigma_T + \epsilon\sigma_L$ values are determined, F_2 and $\sigma_{tot}^{\gamma^* p}$ are calculated assuming σ_L to be either zero or the value given by the Vector Dominance Model (VDM), $\sigma_L = K(Q^2/M_V^2)\sigma_T$. M_V is set equal to the mass of the ρ^0 (0.77 GeV) and K to 0.5.

5.5 Systematic uncertainties

To estimate the systematic uncertainties of the measured F_2 values, the following checks were performed. In each case, an aspect of the event selection, reconstruction of kinematic variables, or F_2 determination was modified, the procedure described above was repeated and the change in F_2 noted. (1) The 0.5% uncertainty on the energy scale (see Section 3.1)

gave an effect of approximately 3% for F_2; the non-linearity of the BPC, estimated to be less than 1%, resulted in changes of less than 5%. (2) Varying the absolute position by 0.5 mm produced changes of less than 6%. (3) To estimate the uncertainty due to the electron finding efficiency, the shower width cut was varied by 1 mm yielding a change up to 2% at high y. (4) The uncertainty due to the CAL event selection cuts was checked by varying the CAL energy scale by 3%, changing the CAL minimum cell energy threshold, varying the δ cut by 2 GeV and varying the y_{JB} cut by 0.01. The effect on F_2 is small for moderate y bins, and reaches 6% at high and low y. (5) The estimated uncertainty on the photoproduction background was 30%, obtained from a comparison of the various methods described above. Consequently, the amount of background subtracted was varied by the same amount. The effect on F_2 increases with y, reaching 4% in the highest y bins. (6) The fraction of diffractive and VM events was varied by 25%. The effect on F_2 was small except for the lowest y points where it reached 4%. (7) Uncertainties due to the description of the hadronic final state in the simulation were estimated by comparing the results from different simulation programs(EPSOFT [34], PYTHIA [35], HERWIG [36]); constraints were provided by comparing hadronic distributions measured in the data with those predicted by the simulations. An error of 2% in F_2 for y less than 0.4, rising linearly to 5% at $y = 0.74$, was assigned. (8) The uncertainties in the radiative corrections, which modify the Born cross-section by 10-15%, were investigated. As mentioned in section 3.1, the tail of the E_{BPC}/E_{calc} distribution for elastic ρ^0 events (figure 1(c)) is due to initial state radiation. Comparison of the simulation with data in that region provides an estimate of the uncertainty in the radiative correction. This uncertainty represents possible changes of 3 to 4% on F_2.

The extracted uncertainties after each of the above systematic checks are displayed in table A (see Appendix). The total systematic error for each bin was determined by adding the changes to F_2 from different checks in quadrature. These are shown in table 1. The systematic errors are around 6% for moderate y bins and are dominated by BPC calibration and radiative correction uncertainties. For low y, uncertainties in the CAL energy scale, as well as the dependence of the acceptance on the fraction of diffractive events leads to uncertainties up to 11%. At high y, uncertainties on the contributions from photoproduction background and the properties of the hadronic final state resulted in errors as high as 8%.

The uncertainties in the luminosity measurement and trigger efficiency contribute to the overall normalisation error, which amounts to 2.4%. The statistical errors are in the range 2–4%.

6 Results

In the following, F_2 is presented as a function of x (or y) and Q^2, and $\sigma_{tot}^{\gamma^* p}$ as a function of W^2 and Q^2. While the former vanishes as $Q^2 \to 0$, the latter is expected to extrapolate smoothly to the total photoproduction cross-section.

The F_2 results are displayed in table 1 in bins of Q^2 and y and plotted in figure 3 as a function of x for different Q^2 bins. Here F_L is assumed to be zero. Assuming F_L as given

Q^2	y	F_2	$\Delta F_2[F_L]$	Q^2	y	F_2	$\Delta F_2[F_L]$
0.11	0.60	0.163±0.005 ± 0.011	0.005	0.25	0.60	0.267±0.010 ± 0.020	0.017
0.11	0.70	0.174±0.006 ± 0.014	0.008	0.30	0.12	0.263±0.005 ± 0.022	0.000
0.15	0.40	0.188±0.006 ± 0.015	0.003	0.30	0.20	0.280±0.005 ± 0.014	0.002
0.15	0.50	0.203±0.005 ± 0.013	0.005	0.30	0.26	0.295±0.007 ± 0.017	0.003
0.15	0.60	0.200±0.006 ± 0.014	0.008	0.30	0.33	0.296±0.008 ± 0.019	0.005
0.15	0.70	0.205±0.008 ± 0.018	0.012	0.30	0.40	0.301±0.010 ± 0.018	0.008
0.20	0.26	0.225±0.005 ± 0.016	0.002	0.30	0.50	0.305±0.011 ± 0.021	0.014
0.20	0.33	0.227±0.006 ± 0.011	0.003	0.40	0.12	0.332±0.007 ± 0.027	0.001
0.20	0.40	0.231±0.005 ± 0.013	0.005	0.40	0.20	0.337±0.008 ± 0.020	0.002
0.20	0.50	0.238±0.006 ± 0.015	0.008	0.40	0.26	0.367±0.010 ± 0.020	0.005
0.20	0.60	0.254±0.009 ± 0.017	0.013	0.40	0.33	0.358±0.012 ± 0.020	0.008
0.20	0.70	0.257±0.011 ± 0.021	0.019	0.40	0.40	0.392±0.014 ± 0.024	0.013
0.25	0.20	0.249±0.005 ± 0.012	0.001	0.50	0.12	0.351±0.009 ± 0.027	0.001
0.25	0.26	0.256±0.005 ± 0.013	0.002	0.50	0.20	0.375±0.010 ± 0.019	0.003
0.25	0.33	0.264±0.006 ± 0.015	0.004	0.50	0.26	0.414±0.013 ± 0.021	0.006
0.25	0.40	0.276±0.007 ± 0.019	0.006	0.65	0.12	0.386±0.012 ± 0.039	0.001
0.25	0.50	0.275±0.009 ± 0.018	0.011	0.65	0.20	0.464±0.018 ± 0.022	0.004

Table 1: Measured F_2 values, with the assumption $F_L = 0$. The first error indicates the statistical error, and the second indicates the systematic error. The values in the column marked $\Delta F_2[F_L]$ show the change in F_2 assuming a value for F_L given by VDM (see text), and are not included in the systematic errors. The bin boundaries in y are 0.08, 0.16, 0.23, 0.30, 0.37, 0.45, 0.54, 0.64, and 0.74 and in Q^2 0.1, 0.13, 0.17, 0.21, 0.27, 0.35, 0.45, 0.58, and 0.74 GeV^2.

by VDM, the effect on F_2 is typically around 1-2% for most bins, and increases F_2 by up to 7% in the lowest x bins, as shown in table 1.

Also shown in figure 3 are the data from the E665[18] experiment at similar Q^2, but much larger x values, and four recent points from the H1[17] experiment with $Q^2 \leq 0.65$ GeV^2. One observes a rise of F_2 by a factor 1.5 to 2 from x near 10^{-3} to x around 10^{-5}. In the bottom of figure 3, the F_2 values for Q^2 =1.5, 3.0 and 6.5 GeV^2 are shown, taken from previous H1 and ZEUS publications [3, 4, 17] and from E665. They illustrate the rapid rise of F_2 with decreasing x as Q^2 increases.

Curves from various theoretical models are overlaid. In general DL and CKMT predictions are 15% and 10% lower than the data respectively, while the BK prediction is 15% higher. No attempt was made to modify the parameters of these models to fit the data. The value of F_2 given by GRV is approximately 35% of the measured value at $Q^2 = 0.4$ GeV^2, rising to about 80% at $Q^2 = 0.65$ GeV^2. At larger Q^2 the GRV predictions reproduce the rapid rise of F_2, but tend to lie somewhat above the data. The ABY parametrisation, which

included preliminary ZEUS BPC F_2 results in the parameter fit, gives a good description of the data.

Figure 4 shows $\sigma_{tot}^{\gamma^* p}$ at low Q^2 and at higher Q^2 taken from previous ZEUS analyses and from the H1 and E665 experiments as a function of W^2. The total cross-section for real γp scattering is also shown [37, 38, 39]. The curves in figure 4 show the expectations from the soft Pomeron model of DL (dotted curve) and the pQCD model of GRV (dashed curve). The W dependence of the DL predictions is given by $\sigma_{tot}^{\gamma^* p} \propto W^{2\lambda}$ with $\lambda = 0.08$ independent of Q^2. The GRV model predicts a stronger variation with Q^2 and W^2. Although the DL model curve is below the ZEUS data, its slope is in broad agreement for $Q^2 \leq 0.65$ GeV^2; however, this is not true for $Q^2 \geq 1.5$ GeV^2. For $Q^2 \geq 1.5$ GeV^2, the GRV model produces a rapid rise of $\sigma_{tot}^{\gamma^* p}$ with W^2 that is in better agreement with the data.

7 Conclusions

In previous studies, ZEUS and H1 have shown that for $Q^2 \geq 1.5$ GeV^2 and $x \ll 10^{-2}$, the proton structure function F_2 rises rapidly as x decreases, in agreement with models based on perturbative QCD. In this paper we have presented a measurement of F_2 and $\sigma_{tot}^{\gamma^* p}$ for $0.11 \leq Q^2 \leq 0.65$ GeV^2 and $2 \times 10^{-6} \leq x \leq 6 \times 10^{-5}$ ($100 < W < 230$ GeV), covering the region between deep inelastic scattering and photoproduction. Similar results have recently been reported by H1[17]. In combination with data from E665 for $x \geq 10^{-3}$, F_2 exhibits a modest rise in this low Q^2 region. Together with previously published HERA data for $Q^2 \geq 1.5$ GeV^2, where the rise is more rapid, our results suggest that pQCD calculations can account for a significant fraction of the cross-section starting at $Q^2 \approx 1$ GeV^2.

Acknowledgements

We thank the DESY Directorate for their strong support and encouragement and the diligent efforts of the HERA machine group. We are also grateful for the support of the DESY computing and network services. The design, construction, and installation of the ZEUS detector has been made possible by the ingenuity and dedicated effort of many people from DESY and the home institutes who are not listed as authors. In particular, we would like to thank M. Gospic, H. Grönstege, J. Hauschildt, K. Löffler, M. Riera, H. Schult, W. Sippach, E. Weiss for their important contributions to the construction and installation of the BPC.

References

[1] ZEUS Collaboration, M. Derrick *et al.*, Phys. Lett. B316 (1993) 412.

[2] H1 Collaboration, I. Abt *et al.*, Nucl. Phys. B407 (1993) 515.

[3] ZEUS Collaboration, M. Derrick *et al.*, Z. Phys. C69 (1996) 607;
ZEUS Collaboration, M. Derrick *et al.*, Z. Phys. C72 (1996) 399.

[4] H1 Collaboration, S. Aid *et al.*, Nucl. Phys. B470 (1996) 3.

[5] M. Glück, E. Reya and A. Vogt, Z. Phys. C48 (1990);
M. Glück, E. Reya and A. Vogt, Z. Phys. C53 (1992) 127;
M. Glück, E. Reya and A. Vogt, Z. Phys. C67 (1995) 433.

[6] V. N. Gribov and L. N. Liptov, Sov. J. Nucl. Phys. 15 (1972) 438, 675;
L. N. Liptov, Sov. J. Nucl. Phys. 20 (1975) 95;
Y. L. Dokshitzer, Sov. Phys. JETP 46 (1977) 641;
G. Altarelli and G. Parisi, Nucl. Phys. B126 (1977) 298.

[7] A. D. Martin, W. J. Stirling and R. G. Roberts, Phys. Rev. D50 (1994) 6734;
A. D. Martin, W. J. Stirling and R. G. Roberts, Phys. Lett. B354 (1995) 155.

[8] CTEQ Collaboration, J. Botts *et al.*, Phys. Lett. B304 (1993) 15.

[9] A. Donnachie and P.V. Landshoff, Phys. Lett. B296 (1992) 227.

[10] A. Donnachie and P.V. Landshoff, Z. Phys. C61 (1994) 139.

[11] A. Capella, A. Kaidalov, C. Merino, and J. Tran Thanh Van, Phys. Lett. B337 (1994) 358.

[12] B. Badelek and J. Kwiecinski, Phys. Lett. B295 (1992) 263.

[13] K. Adel, F. Barreiro, and F.J. Ynduráin, FTUAM 96-39, hep-ph 9610380.

[14] H. Abramowicz *et al.*, Phys. Lett. B269 (1991) 465.

[15] A. Levy, hep-ex 9608009 and TAUP 2349-96.

[16] M. Löwe, Ph.D. thesis of University of Hamburg, DESY-F35D-96-03.

[17] H1 Collaboration, I. Abt *et al.*, DESY-97-042 and hep-ex 9703012.

[18] E665 Collaboration, M.R. Adams *et al.*, Phys. Rev. D54 (1996) 3006.

[19] ZEUS Collaboration, 'The Zeus Detector', Status Report 1993, ed U. Holm, DESY.

[20] A Nucl. Inst. Meth. paper in preparation on the BPC design and performance.

[21] R. Brun *et al.*, CERN DD/EE/84-1 (1987).

[22] R. L. Ford and W. R. Nelson, SLAC 210 (1978);
W. R. Nelson, H. Hiryama and D. W. Rogers, SLAC 265 (1985).

[23] ZEUS Collaboration, M. Derrick *et al.*, Z. Phys. C65 (1995) 379.

[24] N. Harnew *et al.*, Nucl. Instr. Meth. A279 (1989);
B. Foster *et al.*, Nucl. Instr. Meth. A338 (1994) 254.

[25] U. Behrens *el al.*, DESY-92-064.

[26] T. C. Awes *et al.*, Nucl. Inst. Meth. A311 (1992) 130.

[27] J. Andruszkow *et al.*, DESY-92-066.

[28] W. H. Smith *et al.*, Nucl. Inst. Meth. A355 (1995) 278.

[29] A. Kwiatkowski *et al.*, Proceedings of the HERA Workshop, Vol.3 (1991) 1294, Ed. W. Buchmüller and G. Ingelman.

[30] L. Lönnblad, Comp. Phys. Comm. 71 (1992) 15;
L. Lönnblad, Z. Phys. C65 (1995) 285.

[31] G. Ingelman, A. Edin, and J.Rathsman, DESY 96-057.

[32] M. Bergtsson and T. Sjöstrand, Comp. Phys. Comm 43 (1987) 367.

[33] ZEUS Collaboration, M. Derrick *et al.*, Conf. Proc. of ICHEP'96, pa02-053.

[34] M. Kasprzak, Ph.D. Thesis, Warsaw University, DESY F35D-96-16(1996).

[35] H.U. Bengtsson and T. Sjöstrand, Comp. Phys. Comm. 46 (1987) 43;
T. Sjöstrand, CERN Th-7112-93, (1994).

[36] G. Marchesini *et al.*, Comp. Phys. Comm. 67 (1992) 465.

[37] ZEUS Collaboration, M. Derrick *et al.*, Z. Phys. C63 (1994) 391.

[38] H1 Collaboration, S. Aid *et al.*, Z. Phys. C69 (1995) 27.

[39] D. O. Caldwell *et al.*, Phys. Rev. Lett. 40 (1978) 1222;
S. I. Alekhin *et al.*, CERN-HERA 87-01 (1987).

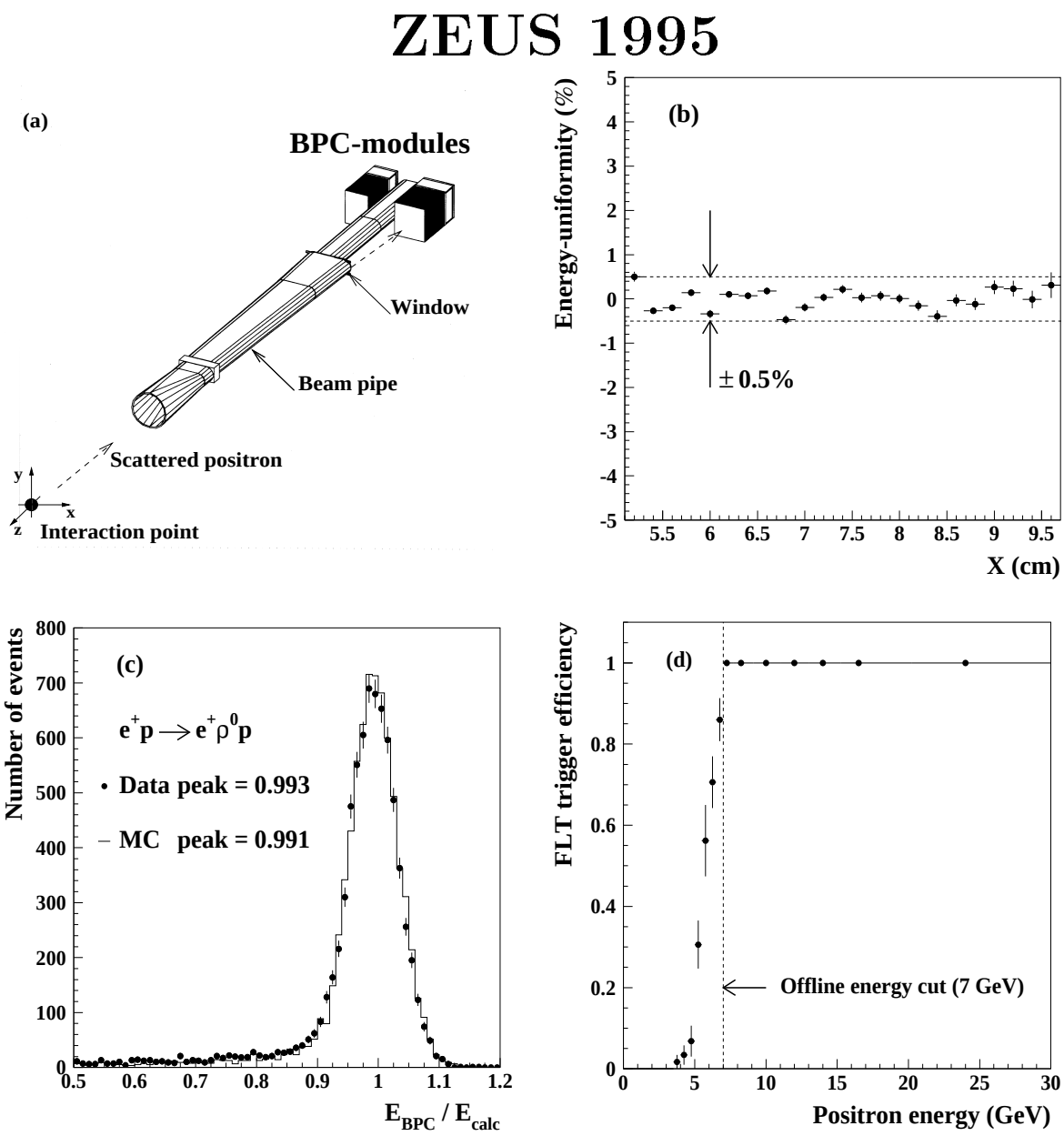

Figure 1: (a) Schematic layout of the BPC and the beampipe. The BPC is located at Z=-2937 mm, and the inner edge is at X=44 mm. (b) The fractional deviation from the mean energy for KP events as a function of the scattered positron X impact position at the BPC. (c) A comparison between MC and data of the ratio of the measured positron energy in the BPC, E_{BPC}, to the calculated positron energy, E_{calc} for elastic ρ^0 events. (d) The FLT trigger efficiency as a function of BPC energy.

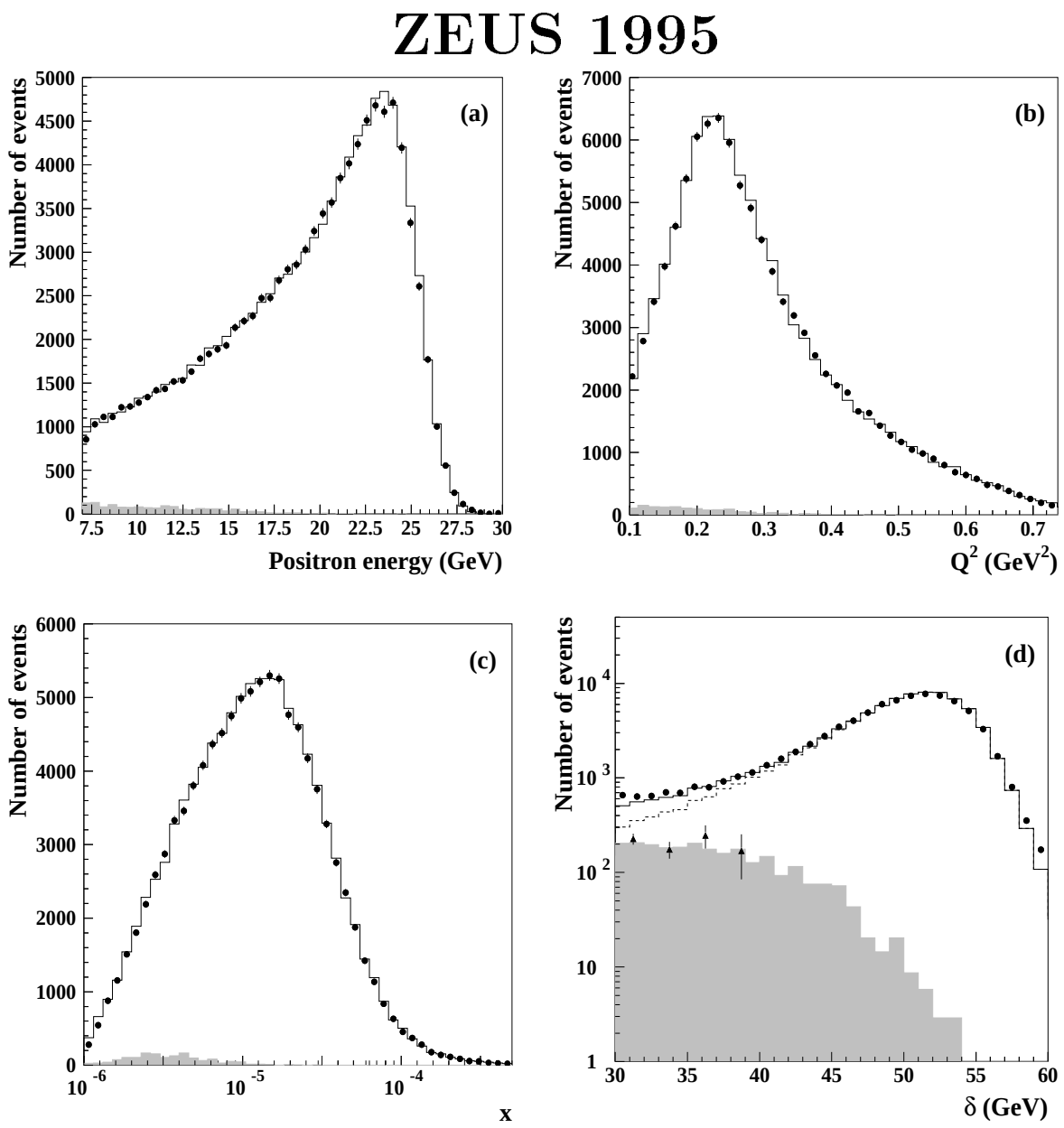

Figure 2: Comparisons between simulated and data distributions for the variables: (a) scattered positron energy; (b) Q^2; (c) x; and (d) δ . Data are shown as solid circles, photoproduction simulation as shaded regions, and the sum of the signal and photoproduction simulations as solid lines. In figure (d) the signal simulation is shown as a dashed line and the measured background as triangular points. The structure function in the simulation has been reweighted to that measured in the present analysis.

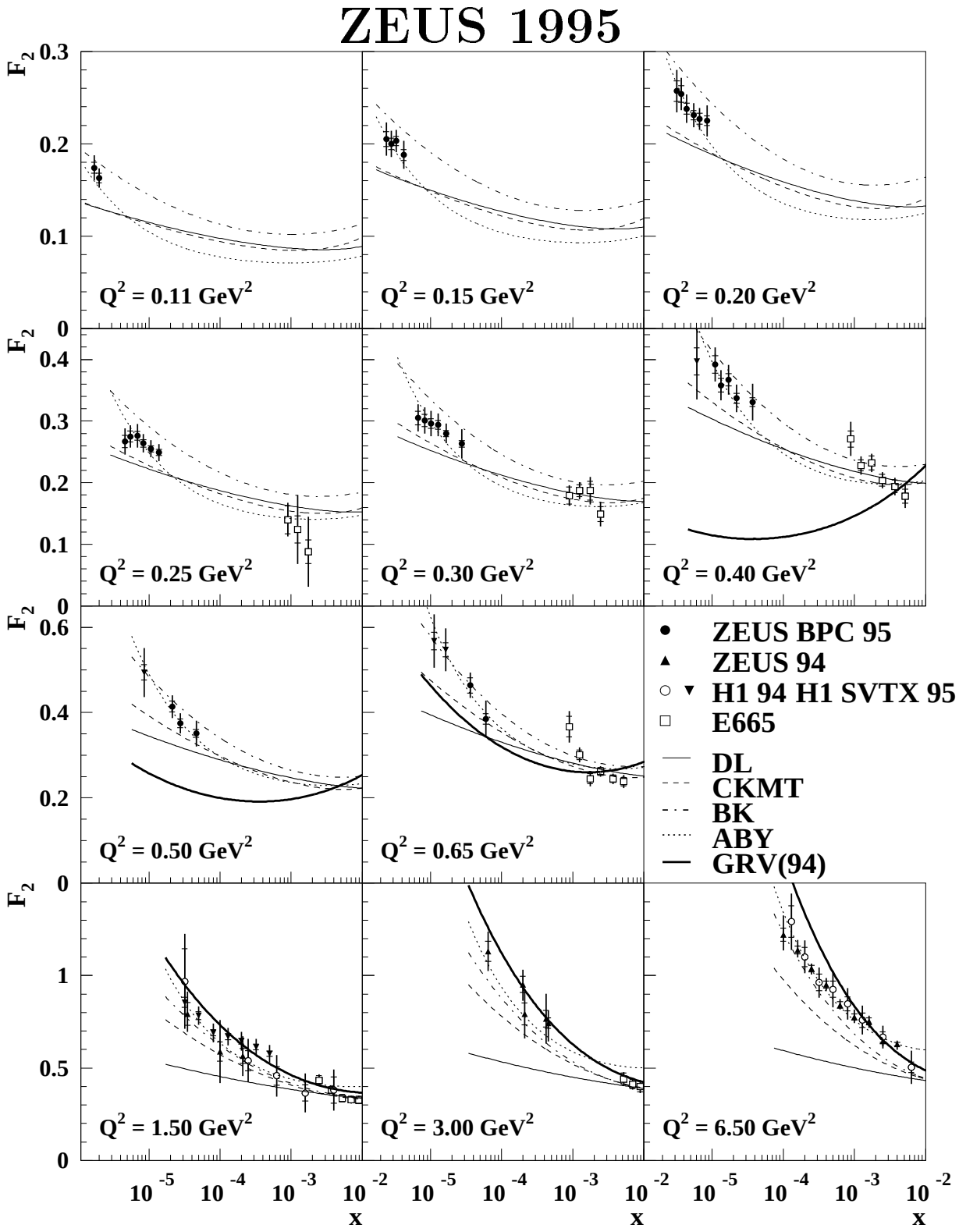

Figure 3: $F_2(x, Q^2)$ as a function of x for different Q^2 bins. The data from this analysis, ZEUS BPC 95, are shown as solid dots, with E665, H1 and previous ZEUS points shown as open squares, open circles and solid triangles, respectively. New points from H1[17] at low Q^2 are also shown as solid inverted triangles (the point at $Q^2 = 0.35$ GeV^2 is displayed in the 0.4 GeV^2 panel; additional points at 2.5 and 3.5 GeV^2 not shown.) Curves from the models of DL, CKMT, BK, ABY and GRV are overlaid.

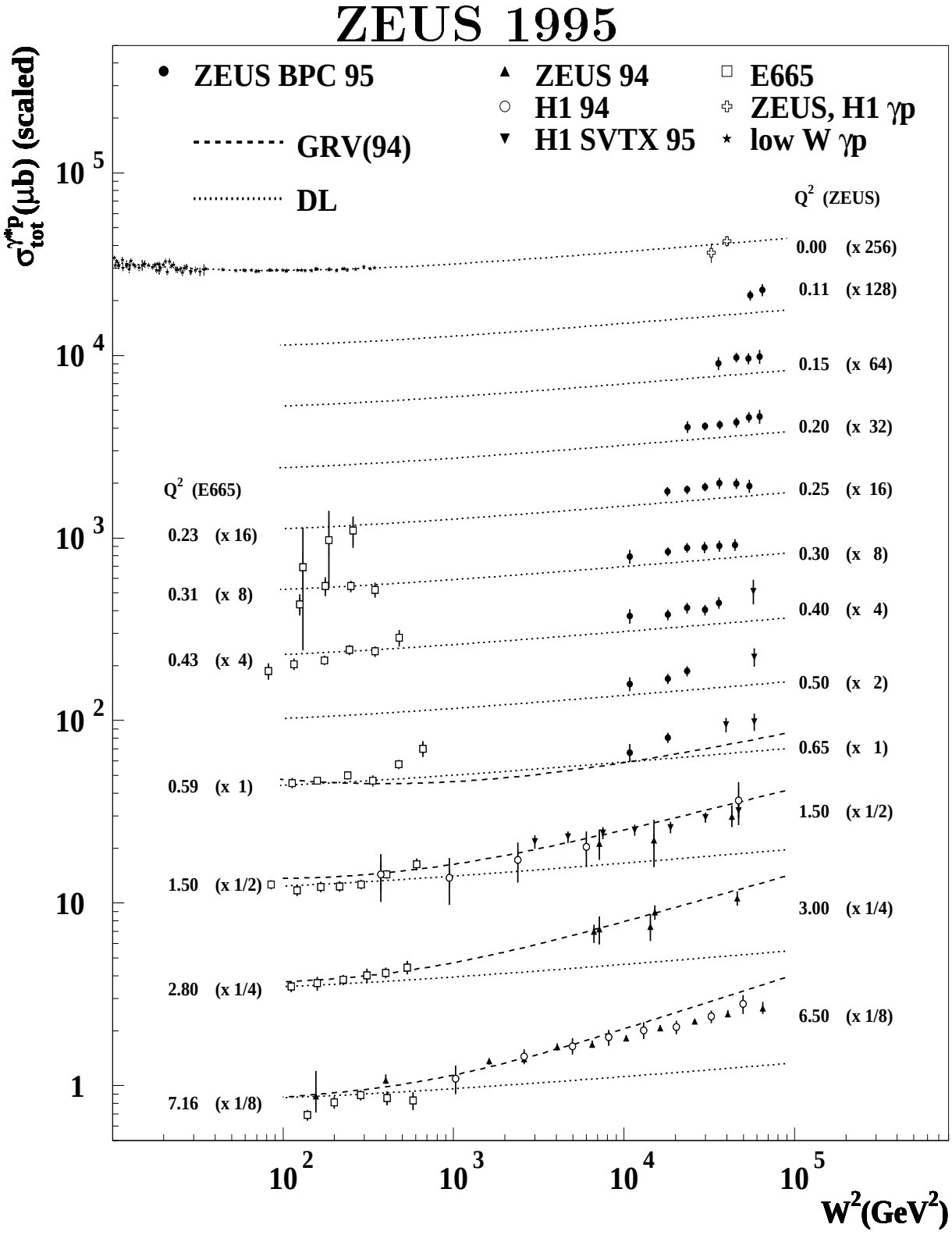

Figure 4: The total virtual photon-proton cross-section $\sigma^{\gamma^* p}_{tot}$ as a function of W^2. The data from this analysis (ZEUS BPC 95), previous 1994 ZEUS analyses, H1, and E665 are shown. The total cross-section for real photon-proton scattering from ZEUS, H1 and photoproduction experiments at low W are also shown. The predictions of DL and GRV (at the ZEUS Q^2 values) are indicated by the dotted and dashed curves respectively.

Appendix A: individual effects of systematic uncertainties

Q^2 (GeV^2)	y	nominal F_2	BPC energy scale +	BPC energy scale -	CAL energy scale +	CAL energy scale -	y_{JB} cut +	y_{JB} cut -	positron identification +	positron identification -	non-linearity of BPC energy scale +	non-linearity of BPC energy scale -	BPC position alignment +	BPC position alignment -	CAL noise cuts +	CAL noise cuts -	δ cut +	δ cut -	photoproduction background +	photoproduction background -	fraction of diffractive events +	fraction of diffractive events -	acceptance from the simulation +	acceptance from the simulation -	radiative corrections +	radiative corrections -
0.11	0.60	0.163	0.91	-0.91	-1.03	1.03	-0.03	0.03	0.20	-0.20	-2.26	2.26	-1.55	1.55	-0.01	0.01	1.18	-1.18	1.34	-1.34	1.10	-1.10	4.00	-4.00	3.82	3.82
0.11	0.70	0.174	1.20	-1.20	-2.48	2.48	0.03	-0.03	0.41	-0.41	-1.82	1.82	2.22	-2.22	0.05	-0.05	-1.62	1.62	2.51	-2.51	1.41	-1.41	5.00	-5.00	3.40	3.40
0.15	0.40	0.188	0.24	-0.24	-0.42	0.42	-0.14	0.14	0.65	-0.65	-1.53	1.53	6.15	6.15	-0.13	0.13	0.03	-0.03	0.60	-0.60	0.28	-0.28	2.00	-2.00	4.00	4.00
0.15	0.50	0.203	1.53	-1.53	-0.46	0.46	-0.22	0.22	1.18	-1.18	-2.98	2.98	0.52	-0.52	0.44	-0.44	1.93	-1.93	0.78	-0.78	0.21	-0.21	3.00	-3.00	4.03	4.03
0.15	0.60	0.200	-0.66	0.66	-0.95	0.95	-0.18	0.18	0.78	-0.78	-0.16	0.16	3.53	-3.53	0.03	-0.03	0.47	-0.47	2.01	-2.01	0.91	-0.91	4.00	-4.00	3.82	3.82
0.15	0.70	0.205	1.17	-1.17	-1.80	1.80	-0.10	0.10	-0.27	0.27	-2.22	2.22	2.77	-2.77	-0.77	0.77	-1.42	1.42	3.53	-3.53	2.24	-2.24	5.00	-5.00	3.40	3.40
0.20	0.26	0.225	2.62	-2.62	-0.43	0.43	-0.01	0.01	-0.18	0.18	-2.94	2.94	4.21	4.21	0.02	-0.02	-0.03	0.03	0.32	-0.32	0.42	-0.42	2.00	-2.00	3.60	3.60
0.20	0.33	0.228	0.97	-0.97	-0.19	0.19	-0.46	0.46	0.30	-0.30	-0.86	0.86	0.76	-0.76	-0.32	0.32	-0.03	0.03	0.45	-0.45	0.19	-0.19	2.00	-2.00	3.86	3.86
0.20	0.40	0.231	0.31	-0.31	-0.32	0.32	-0.38	0.38	0.55	-0.55	-2.21	2.21	2.29	-2.29	-0.37	0.37	0.22	-0.22	0.88	-0.88	0.33	-0.33	2.00	-2.00	4.00	4.00
0.20	0.50	0.238	0.35	-0.35	-0.43	0.43	-0.37	0.37	0.58	-0.58	-2.30	2.30	2.67	-2.67	-0.41	0.41	-0.51	0.51	1.36	-1.36	1.02	-1.02	3.00	-3.00	4.03	4.03
0.20	0.60	0.254	1.12	-1.12	-0.77	0.77	-0.21	0.21	-0.77	0.77	-2.52	2.52	1.89	-1.89	-0.44	0.44	-0.16	0.16	1.67	-1.67	0.78	-0.78	4.00	-4.00	3.82	3.82
0.20	0.70	0.257	1.39	-1.39	-2.21	2.21	-0.11	0.11	-0.29	0.29	-2.86	2.86	1.27	-1.27	-1.50	1.50	-0.62	0.62	3.14	-3.14	0.80	-0.80	5.00	-5.00	3.40	3.40
0.25	0.20	0.249	1.75	-1.75	-0.92	0.92	-0.20	0.20	-0.64	0.64	-0.90	0.90	0.91	-0.91	-0.18	0.18	0.00	0.00	0.37	-0.37	0.95	-0.95	2.00	-2.00	3.30	3.30
0.25	0.26	0.256	1.65	-1.65	-0.22	0.22	-0.33	0.33	-0.77	0.77	-1.86	1.86	1.83	-1.83	-0.28	0.28	0.00	0.00	0.43	-0.43	0.50	-0.50	2.00	-2.00	3.60	3.60
0.25	0.33	0.264	0.70	-0.70	-0.29	0.29	-0.43	0.43	-0.90	0.90	-2.81	2.81	1.98	-1.98	-0.43	0.43	-0.01	0.01	0.67	-0.67	0.61	-0.61	2.00	-2.00	3.86	3.86
0.25	0.40	0.276	1.60	-1.60	-0.02	0.02	-0.79	0.79	-0.53	0.53	-3.55	3.55	2.71	-2.71	-0.45	0.45	0.15	-0.15	1.05	-1.05	0.45	-0.45	2.00	-2.00	4.00	4.00
0.25	0.50	0.275	-0.02	0.02	-0.56	0.56	-0.37	0.37	-0.23	0.23	-1.90	1.90	3.46	-3.46	-0.33	0.33	0.40	-0.40	1.16	-1.16	0.67	-0.67	3.00	-3.00	4.03	4.03
0.25	0.60	0.267	-0.60	0.60	-1.38	1.38	-0.26	0.26	-0.49	0.49	-0.15	0.15	3.47	-3.47	0.22	-0.22	1.05	-1.05	3.14	-3.14	1.16	-1.16	4.00	-4.00	3.82	3.82
0.30	0.12	0.263	-1.42	1.42	-4.24	4.24	1.41	-1.41	0.57	-0.57	4.14	-4.14	1.57	-1.57	2.62	-2.62	-0.04	0.04	-0.26	0.26	3.20	-3.20	2.00	-2.00	2.76	2.76
0.30	0.20	0.280	0.56	-0.56	-0.74	0.74	-0.12	0.12	-1.01	1.01	0.21	-0.21	2.75	-2.75	-0.25	0.25	0.04	-0.04	0.39	-0.39	1.35	-1.35	2.00	-2.00	3.30	3.30
0.30	0.26	0.295	1.42	-1.42	-0.17	0.17	-0.41	0.41	-1.12	1.12	-2.04	2.04	2.65	-2.65	-0.40	0.40	0.05	-0.05	0.53	-0.53	0.26	-0.26	2.00	-2.00	3.60	3.60
0.30	0.33	0.296	1.53	-1.53	0.00	0.00	-0.79	0.79	-0.69	0.69	-3.22	3.22	2.73	-2.73	-0.70	0.70	0.10	-0.10	0.67	-0.67	-0.19	0.19	2.00	-2.00	3.86	3.86
0.30	0.40	0.301	1.30	-1.30	-0.18	0.18	-0.53	0.53	-0.61	0.61	-2.41	2.41	2.88	-2.88	-0.55	0.55	0.07	-0.07	0.84	-0.84	0.48	-0.48	2.00	-2.00	4.00	4.00
0.30	0.50	0.305	1.68	-1.68	-0.42	0.42	-0.35	0.35	1.20	-1.20	-3.44	3.44	1.49	-1.49	-0.04	0.04	0.97	-0.97	1.34	-1.34	0.46	-0.46	3.00	-3.00	4.03	4.03
0.40	0.12	0.332	-1.54	1.54	-4.11	4.11	0.96	-0.96	0.36	-0.36	4.28	-4.28	2.42	-2.42	1.95	-1.95	-0.03	0.03	-0.22	0.22	2.94	-2.94	2.00	-2.00	2.76	2.76
0.40	0.20	0.337	2.09	-2.09	-0.70	0.70	-1.19	1.19	-1.02	1.02	-1.75	1.75	2.77	-2.77	-0.85	0.85	0.10	-0.10	0.47	-0.47	0.76	-0.76	2.00	-2.00	3.30	3.30
0.40	0.26	0.367	1.07	-1.07	0.01	-0.01	-0.20	0.20	-1.26	1.26	-1.37	1.37	2.77	-2.77	-0.24	0.24	0.12	-0.12	0.49	-0.49	0.10	-0.10	2.00	-2.00	3.60	3.60
0.40	0.33	0.358	0.48	-0.48	-0.19	0.19	-0.81	0.81	-1.03	1.03	-2.14	2.14	2.38	-2.38	-0.71	0.71	0.12	-0.12	0.74	-0.74	-0.27	0.27	2.00	-2.00	3.86	3.86
0.40	0.40	0.392	1.38	-1.38	-0.09	0.09	-0.49	0.49	-1.90	1.90	-2.69	2.69	1.58	-1.58	-0.47	0.47	0.10	-0.10	1.08	-1.08	0.01	-0.01	2.00	-2.00	4.00	4.00
0.50	0.12	0.351	-1.35	1.35	-3.87	3.87	-0.16	0.16	0.28	-0.28	3.80	-3.80	2.78	-2.78	1.09	-1.09	-0.05	0.05	-0.24	0.24	2.64	-2.64	2.00	-2.00	2.76	2.76
0.50	0.20	0.375	0.33	-0.33	-0.82	0.82	-0.79	0.79	-0.85	0.85	0.41	-0.41	2.69	-2.69	-0.53	0.53	0.11	-0.11	0.37	-0.37	0.77	-0.77	2.00	-2.00	3.30	3.30
0.50	0.26	0.414	0.74	-0.74	0.16	-0.16	-0.84	0.84	-1.74	1.74	-0.34	0.34	2.09	-2.09	-0.37	0.37	0.14	-0.14	0.55	-0.55	0.59	-0.59	2.00	-2.00	3.60	3.60
0.65	0.12	0.386	-2.83	2.83	-4.34	4.34	3.14	-3.14	0.44	-0.44	5.25	-5.25	2.61	-2.61	3.46	-3.46	-0.07	0.07	-0.18	0.18	2.60	-2.60	2.00	-2.00	2.76	2.76
0.65	0.20	0.464	1.68	-1.68	-0.42	0.42	0.75	-0.75	-1.00	1.00	-1.04	1.04	1.35	-1.35	0.45	-0.45	0.22	-0.22	0.52	-0.52	0.67	-0.67	2.00	-2.00	3.30	3.30

Table A: The determination of the systematic errors was discussed in section 5.5. Q^2, y, and measured F_2 values are listed in columns 1 to 3. The individual effects of each of the systematic checks on F_2 are displayed (in percentages of F_2) in columns 4 to 27.